Modeling and Stability Enhancement Method of Wireless Motor System Based on Damping Reconstruction Control

Shuai Dong, Yuebo Chen, Xiangyu Chen, Baichuan Zhang, and Chunbo Zhu

***Abstract*—The wireless motor system eliminates the electrical connection between the power supply and the motor, ensuring high reliability and low maintenance. However, the resonance between the secondary side inductor and the dc-link capacitor, interacting with the motor drive with negative impedance characteristics, causes oscillation and instability in the dc-link voltage. This phenomenon manifests as the control-to-output function having right-half-plane poles. This article establishes an equivalent model of the wireless motor system using the short-time Fourier transform and analyzes the main factors affecting system stability. Additionally, a control strategy for implementing damping reconstruction control on the secondary side is proposed, aiming to improve system stability by equivalently increasing the secondary side coil internal resistance, thereby efficiently decreasing the system's reliance on dc-link capacitor value. Simulation and experimental results validate the effectiveness of the proposed damping reconstruction control method. This article is accompanied by a video file demonstrating the experimental operations under different operating conditions.**

***Index Terms*—Active damping, motor drive, stability, wireless power transfer.**

NOMENCLATURE

$L_{\mathrm{p\_c}}$	Primary side compensation inductance.
$C_{\mathrm{p\_p}}$	Primary side parallel capacitance.
$C_{\mathrm{p\_s}}$	Primary side series capacitance.
L_{p}	Primary side coil inductance.
L_{s}	Secondary side coil inductance.
C_{s}	Secondary side compensation capacitance.
M	Magnetic coupler mutual inductance.
R_{p}	Primary side coil internal resistance.
R_{s}	Secondary side coil internal resistance.
C_{dc}	DC-link capacitance.
R_{L}	Motor load.
U_{in}	DC input voltage.
u_{p}	Primary side inverter output voltage.
u_{s}	Secondary side rectifier input voltage.
$u_{\mathrm{s\_ind}}$	Secondary side coil induced voltage.
u_{dc}	DC-link voltage.
i_{p}	Primary side coil current.
i_{s}	Secondary side coil current.
i_{rec}	Secondary side rectifier output current.
$i_{\mathrm{s\_pk}}$	Secondary side coil current peak.
i_{inv}	Motor inverter input current.
P	Motor output power.
ω	Primary side switching angular frequency.
ω_{r}	System resonance angular frequency.
θ	Primary side inverter phase shift Angle.
Subscript F	Fourier series for the corresponding variable.
Subscript 0	Steady-state value of the corresponding variable.
L_{ω}	Equivalent inductance of the secondary side $L_{\mathrm{s}}C_{\mathrm{s}}$ series circuit.
$\Delta\omega$	Difference between ω and ω_{r}.
$i_{\mathrm{s\_Re}}$	Real part of the first Fourier series of the secondary side current.
$i_{\mathrm{s\_Im}}$	Imaginary part of the first Fourier series of the secondary side current.

I. INTRODUCTION

THE wireless motor system represents an innovative integration of wireless power transfer (WPT) and motor drive systems. Unlike conventional motor drive methods, coupling coils and compensation networks replace power cables in supplying power to motor drivers. This approach benefits from achieving electrical isolation between the power source and the motor, avoiding damage caused by wire movement. The wireless motor system demonstrates significant potential in a range of applications, such as mobile platforms, electric vehicles, pipeline valves, and robotic articulations [1], [2], [3], [4].

Typical system setups often incorporate the use of supercapacitors or batteries to manage energy flow and stabilize voltage [2], [5]. This approach notably contributes to an increase in the system's size, weight, and cost. Furthermore, these components tend to have lifespan limitations due to environmental factors like low temperatures and humidity. By eliminating the need for batteries and integrating smaller film capacitors instead, these issues can be effectively addressed.

Manuscript received 21 November 2023; revised 7 February 2024 and 8 May 2024; accepted 7 June 2024. Date of publication 18 June 2024; date of current version 16 July 2024. This work was supported by the National Natural Science Foundation of China under Grant 51807032. Recommended for publication by Associate Editor S. Khajehoddin. *(Corresponding author: Yuebo Chen.)*

Shuai Dong, Yuebo Chen, Xiangyu Chen, Baichuan Zhang, and Chunbo Zhu are with the School of Electrical Engineering and Automation, Harbin Institute of Technology, Harbin 150000, China, and also with the Zhengzhou Research Institute of Harbin Institute of Technology, Zhengzhou 450000, China (e-mail: 21S106168@stu.hit.eud.cn).

This article has supplementary material provided by the authors and color versions of one or more figures available at https://doi.org/10.1109/TPEL.2024.3415648.

Digital Object Identifier 10.1109/TPEL.2024.3415648

For example, this system can be used in patrol robots. By eliminating the battery component and using smaller film capacitors, it is possible to solve the battery lifespan issue in harsh environments. This adjustment leads to a solution that is not only more efficient and reliable but also more cost-effective, with the added advantage of reduced overall size.

However, under the influence of the motor controller, the motor and driver can be equated to a constant power load (CPL), exhibiting "negative impedance" characteristics, with the driver's input current decreasing as the dc-link voltage increases [6], [7], [8]. The removal of the secondary-side battery component results in a closer connection between the WPT system and the motor drive system. When the output power increases due to a rise in speed or torque, this "negative impedance" characteristic causes a reduction in the damping of the wireless motor system. Insufficient system damping could lead to the presence of right-half-plane (RHP) poles in its control-to-output transfer function, thereby jeopardizing system stability. The resonance between the secondary side inductor and the dc-link capacitor, interacting with the motor drive with negative impedance characteristic, causes oscillation and instability in the dc-link voltage. This type of oscillation will severely affect the normal operation of the system. Typically, passive damping circuits, such as *RC* parallel, *RL* parallel, and *RL* series, are designed to enhance system stability [9], [10]. However, this approach not only increases the system's size, cost, and losses but also reduces its bandwidth.

Researchers have delved into the application of active damping techniques as a means to enhance the stability of CPL systems. This approach fundamentally aims to improve system damping through various control measures, predominantly including bus-side, source-side, and load-side controls. In the bus-side control method, auxiliary circuits, like adaptive active capacitors [11], supercapacitors [12], or power buffers [13], are incorporated into the dc-link of the cascaded system to emulate system damping or to inject compensating current, ensuring the dc-link voltage remains stable. However, this method increases the power consumption and complexity of the system. Source-side control stabilizes the system by adjusting the output impedance on the source side, either through widening the control loop bandwidth of the source-side converter [14] or employing virtual damping control [15], [16], thereby achieving impedance matching. In [17], a virtual series *RC* damper was designed in parallel with the source-side capacitor. By modifying the voltage control signal of the source-side converter, the system's instability was overcome. A virtual negative inductor, applied to the source-side converter as described in [18], effectively counteracted the substantial line inductance, subsequently improving system stability.

If the source-side circuit is challenging to control or uncontrollable, load-side control serves as an excellent substitute. This technique involves altering the coefficients of the characteristic equation or incorporating additional virtual damping, achieved by channeling power or current signals into the load-side control circuit. RHP poles can be eliminated by directly adjusting the system's characteristic equation coefficients to meet stability conditions. This ensures stable system operation. Primary methods include reference current injection, reference voltage injection, and small-signal polarity modification. The reference current injection method injects the oscillation component of the dc-link voltage into the current inner loop of the reduced dc-link capacitance motor drive system, suppressing unstable oscillations by dynamically modifying the current reference value [19], [20]. However, if the oscillation frequency of the dc-link voltage surpass the bandwidth of the current inner loop, there may be a resultant decline in the response performance of the current inner loop. The reference voltage injection method injects the oscillation component of the dc-link voltage into the motor's voltage reference value [21], [22], [23], offering faster dynamic response and greater robustness. In [24], the polarity of the small-signal component of the dc-link voltage is altered and injected into the dc-link voltage reference of the modulator. This approach circumvents the need for dynamically acquiring compensation factors contingent upon system parameters and operational conditions, thereby solidifying system stability.

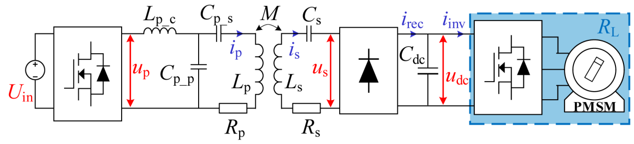

Fig. 1. Wireless motor system topology.

Furthermore, improving system stability can be achieved by introducing additional virtual damping through load-side control. In [25], [26], and [27], the stability of the cascaded system is ensured by connecting an adaptive virtual impedance at the input of the load side. This approach enables adaptive adjustment of the load-side input impedance for various source-side converters. In [28], introducing a virtual capacitor in parallel with the dc-link enhances system damping while simultaneously reducing the actual dc-link capacitor's physical size. In [29], a virtual resistor is connected in parallel across the line inductor in the motor drive system with a reduced dc-link capacitor. By computing virtual current based on the voltage difference between the grid and the dc link, and then injecting it into the motor control loop, system stability is enhanced.

This article introduces a novel secondary side damping reconstruction control (DRC) method suitable for wireless motor systems. It reconstructs the system's damping by equivalently increasing the secondary side coil internal resistance, addressing the issue of wireless motor system instability when input voltage decreases or output power increases. In Section II, the system circuit is simplified, and the small-signal model of the wireless motor system is established. In Section III, the system's stability conditions are provided, and the effects of various parameters are analyzed. In Section IV, the DRC method is presented, along with guidelines for designing the control parameters. In Section V, simulation and experimental results are provided to validate the effectiveness of the control method. Finally, Section VI concludes this article.

II. MODELING ANALYSIS OF WIRELESS MOTOR SYSTEM

The topology of the wireless motor system is shown in Fig. 1. The system comprises a dc power supply, a primary inverter, a magnetic coupler with LCC-S compensation, a secondary rectifier, a dc-link capacitor, a three-phase inverter, and a permanent

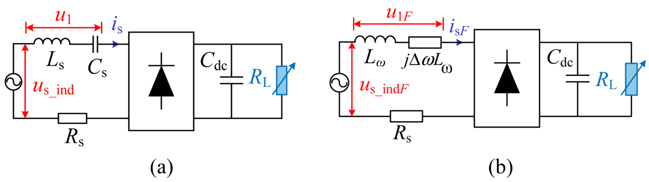

(a) (b)

Fig. 2. Secondary side circuit. (a) Original circuit. (b) Equivalent circuit.

magnet synchronous motor (PMSM). The primary side of the system employs the phase-shifting modulation strategy. Using the phase of the output voltage of the primary inverter as the reference phase, it can be expressed as

$$u_{\mathrm{p}}(t) = \frac{4U_{\mathrm{in}}}{\pi}\cos\theta\sin\omega t. \tag{1}$$

If the output of the motor driver is strictly regulated, its instantaneous input power is constant within the regulation bandwidth [30]. Therefore, from the perspective of the dc link, the motor and driver as a whole behave as a CPL, which can be represented as

$$R_{\mathrm{L}} = \frac{u_{\mathrm{dc}}^2}{P}. \tag{2}$$

A. System Equivalent Circuit

Because the primary side of the system adopts the LCC topology, when the dc input voltage U_{in} is constant, the RMS value I_{p} of the primary side coil current remains constant. Therefore, the expression of I_{p} can be obtained

$$I_{\mathrm{p}} = \frac{U_{\mathrm{p}}}{\omega L_{\mathrm{p\_c}}}. \tag{3}$$

The uppercase letters U and I represent the RMS value of the corresponding ac voltage and current variable, respectively. According to the phase relationship, the primary side coil current i_{p} can be expressed as

$$i_{\mathrm{p}}(t) = -\sqrt{2}I_{\mathrm{p}}\cos\omega t. \tag{4}$$

Therefore, the secondary side coil induced voltage $u_{\mathrm{s\_ind}}$ can be expressed as

$$u_{\mathrm{s\_ind}}(t) = \sqrt{2}U_{\mathrm{s\_ind}}\sin\omega t = \sqrt{2}\omega M I_{\mathrm{p}}\sin\omega t. \tag{5}$$

On combining (1) and (3)–(5), $U_{\mathrm{s\_ind}}$ can be obtained as

$$U_{\mathrm{s\_ind}} = \frac{2\sqrt{2}MU_{\mathrm{in}}}{\pi L_{\mathrm{p\_c}}}\cos\theta. \tag{6}$$

The secondary circuit of the system is shown in Fig. 2(a). The method in [31] is used to equivalent the secondary circuit and the short-time Fourier transform is applied to various voltage and current variables, yielding their Fourier series

$$\begin{cases} u_F(t) = \frac{1}{T}\int_{t-T}^{t} u(\tau)e^{-j\omega\tau}d\tau \\ i_F(t) = \frac{1}{T}\int_{t-T}^{t} i(\tau)e^{-j\omega\tau}d\tau \end{cases}. \tag{7}$$

The derivative of the secondary current $\frac{d}{dt}i_{\mathrm{s}F}(t)$ is

$$\begin{aligned} \frac{di_{\mathrm{s}F}(t)}{dt} &= \frac{d}{dt}\left[\frac{1}{T}\int_{t-T}^{t} i_{\mathrm{s}}(\tau)e^{-j\omega\tau}d\tau\right] \\ &= \frac{1}{T}\int_{t-T}^{t}\left[\frac{di_{\mathrm{s}}(\tau)}{d\tau} - j\omega i_{\mathrm{s}}(\tau)\right]e^{-j\omega\tau}d\tau \\ &= \frac{u_{\mathrm{Ls}F}(t)}{L_{\mathrm{s}}} - j\omega i_{\mathrm{s}F}(t). \end{aligned} \tag{8}$$

The derivative of the compensating capacitor voltage $\frac{d}{dt}u_{C\mathrm{s}F}(t)$ can be obtained in the same way. Hence, the voltage across L_{s} and the current through C_{s} can be expressed as

$$\begin{cases} u_{\mathrm{Ls}F}(t) = L_{\mathrm{s}}\frac{di_{\mathrm{s}F}(t)}{dt} + j\omega L_{\mathrm{s}}i_{\mathrm{s}F}(t) \\ i_{\mathrm{s}F}(t) = C_{\mathrm{s}}\frac{du_{C\mathrm{s}F}(t)}{dt} + j\omega C_{\mathrm{s}}u_{C\mathrm{s}F}(t) \end{cases}. \tag{9}$$

Consider L_{s} and C_{s} as a whole, and the Fourier series of the voltage across them, u_{1F}, is

$$\begin{aligned} u_{1F}(t) &= u_{\mathrm{Ls}F}(t) + u_{C\mathrm{s}F}(t) \\ &= L_{\mathrm{s}}\frac{di_{\mathrm{s}F}(t)}{dt} + j\omega L_{\mathrm{s}}i_{\mathrm{s}F}(t) + u_{C\mathrm{s}F}(t). \end{aligned} \tag{10}$$

The system's switching frequency is much greater than the disturbance frequency of the system input [31], i.e., $\omega >> |s|$. Let $\Delta\omega = \omega$ - ω_{r}, then

$$\begin{aligned} \frac{u_{1F}(s)}{i_{\mathrm{s}F}(s)} &= \frac{(s + j\omega + j\omega_{\mathrm{r}})(s + j\omega - j\omega_{\mathrm{r}})}{s + j\omega}L_{\mathrm{s}} \\ &\approx s\frac{\omega + \omega_{\mathrm{r}}}{\omega}L_s + j\frac{\omega^2 - \omega_{\mathrm{r}}^2}{\omega}L_s \\ &= sL_\omega + j\Delta\omega L_\omega. \end{aligned} \tag{11}$$

As depicted in Fig. 2(b), the secondary side equivalent circuit is derived based on (11). Consequently, the system is simplified and consists of equivalent inductance L_ω, secondary side coil resistance R_{s}, dc-link capacitor C_{dc}, and load R_{L}. This simplification aids in a straightforward analysis of the system's dynamics.

B. System Large-Signal Model

Based on Fig. 2(b), formulate the differential equation

$$\begin{cases} L_\omega\frac{di_{\mathrm{s}F}}{dt} = u_{\mathrm{s\_ind}F} - j\Delta\omega L_\omega i_{\mathrm{s}F} - R_{\mathrm{s}}i_{\mathrm{s}F} - u_{\mathrm{s}F} \\ C_{\mathrm{dc}}\frac{du_{\mathrm{dc}F}}{dt} = i_{\mathrm{rec}F} - \frac{P}{u_{\mathrm{dc}F}} \end{cases}. \tag{12}$$

Retaining only the first-order component, a function *f*(*t*) with period *T* can be expressed as

$$f(t) \approx \frac{a_0}{2} + a_{1c}\cos\omega t + a_{1s}\sin\omega t. \tag{13}$$

Meanwhile, its first-order Fourier series is

$$f_F(t) = \frac{\sqrt{2}}{2}(a_{1c} + ja_{1s}) \tag{14}$$

where a_0, a_{1c}, and a_{1s} represent the DC component, first-order cosine component, and first-order sine component of the function *f*(*t*), respectively. The state variable is defined as

$$\boldsymbol{x} = [x_1 x_2 x_3] = [i_{\mathrm{s\_Re}} i_{\mathrm{s\_Im}} u_{\mathrm{dc}}]^T \tag{15}$$

and the control input variable is defined as

$$\boldsymbol{u} = [\theta]. \tag{16}$$

The rectifier's input–output relationship is

$$\begin{cases} u_{\mathrm{s}} = \frac{4}{\pi}\frac{i_{\mathrm{s}}}{i_{\mathrm{s\_pk}}} u_{\mathrm{dc}} \\ i_{\mathrm{rec}} = \frac{2}{\pi} i_{\mathrm{s\_pk}} = \frac{2}{\pi}\sqrt{i_{\mathrm{s\_Re}}^2 + x_{\mathrm{s\_Im}}^2} \end{cases}. \tag{17}$$

Combining (6) and (12)–(17), the large-signal model of the system's secondary circuit can be obtained

$$\begin{cases} L_\omega \frac{dx_1}{dt} = \Delta\omega L_\omega x_2 - R_{\mathrm{s}} x_1 - \frac{4}{\pi}\frac{x_1}{i_{\mathrm{pk}}} x_3 \\ L_\omega \frac{dx_2}{dt} = \frac{2\sqrt{2}MU_{\mathrm{in}}}{\pi L_{\mathrm{p}}}\cos\theta + \Delta\omega L_\omega x_1 - R_{\mathrm{s}} x_2 - \frac{4}{\pi}\frac{x_2}{i_{\mathrm{pk}}} x_3 \\ C_{\mathrm{dc}}\frac{dx_3}{dt} = \frac{2}{\pi} i_{\mathrm{s\_pk}} - \frac{P}{x_3}. \end{cases} \tag{18}$$

C. System Small-Signal Model

The large signal model is nonlinear. To obtain a linear model that is easy to analyze, a linearization method is used to perturb state variables and control variables near the steady-state operating point. The state variable $\boldsymbol{x}$ and the control input variable $\boldsymbol{u}$ are rewritten as their steady-state values plus some small perturbations as follows:

$$\boldsymbol{x} = \boldsymbol{X} + \hat{\boldsymbol{x}} \tag{19}$$

$$\boldsymbol{u} = \boldsymbol{U} + \hat{\boldsymbol{u}} \tag{20}$$

where $\boldsymbol{X}$ and $\hat{\boldsymbol{x}}$, respectively, represent the steady-state value and the disturbance value of the state variable, and $\boldsymbol{U}$ and $\hat{\boldsymbol{u}}$ represent the steady-state and disturbance value of the input variables, respectively.

Substituting (19)–(20) into (18) and linearizing with Taylor expansion, the small-signal state-space expression of the system can be derived

$$\begin{cases} \dot{\boldsymbol{x}} = \boldsymbol{A}\boldsymbol{x} + \boldsymbol{B}\boldsymbol{u} \\ \boldsymbol{y} = \boldsymbol{C}\boldsymbol{x} \end{cases} \tag{21}$$

where

$$\boldsymbol{A} = \begin{pmatrix} -\frac{4X_2^2X_3}{\pi i_{\mathrm{s\_pk0}}^3 L_\omega} - \frac{R_{\mathrm{s}}}{L_\omega} & \frac{4X_1X_2X_3}{\pi i_{\mathrm{s\_pk0}}^3 L_\omega} + \Delta\omega & -\frac{4X_1}{\pi i_{\mathrm{s\_pk0}} L_\omega} \\ \frac{4X_1X_2X_3}{\pi i_{\mathrm{s\_pk0}}^3 L_\omega} - \Delta\omega & -\frac{4X_1^2X_3}{\pi i_{\mathrm{s\_pk0}}^3 L_\omega} - \frac{R_{\mathrm{s}}}{L_\omega} & -\frac{4X_2}{\pi i_{\mathrm{s\_pk0}} L_\omega} \\ \frac{2X_1}{\pi i_{\mathrm{s\_pk0}} C_{\mathrm{dc}}} & \frac{2X_2}{\pi i_{\mathrm{s\_pk0}} C_{\mathrm{dc}}} & \frac{P}{X_3^2 C_{\mathrm{dc}}} \end{pmatrix}$$

$$\boldsymbol{B} = \begin{pmatrix} 0 & \frac{G_{\mathrm{ps}}}{L_\omega} & 0 \end{pmatrix}^T \quad \boldsymbol{C} = \begin{pmatrix} 0 & 0 & 1 \end{pmatrix}^T$$

$$G_{\mathrm{ps}} = -\frac{2\sqrt{2}MU_{\mathrm{in}}}{\pi L_f}\sin\theta_0.$$

At steady-state, since the secondary side coil current is in phase with the induced voltage, i.e., $X_1 = 0$, the matrix $\boldsymbol{A}$ can be simplified to

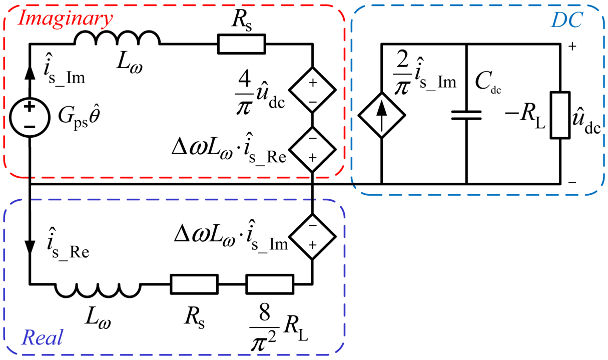

Fig. 3. Small-signal model of the wireless motor system.

$$\boldsymbol{A} = \begin{pmatrix} -\frac{8u_{\mathrm{dc0}}^2}{\pi^2 P L_\omega} - \frac{R_{\mathrm{s}}}{L_\omega} & \Delta\omega & 0 \\ -\Delta\omega & -\frac{R_{\mathrm{s}}}{L_\omega} & -\frac{4}{\pi L_\omega} \\ 0 & \frac{2}{\pi C_{\mathrm{dc}}} & \frac{P}{u_{\mathrm{dc}}^2 C_{\mathrm{dc}}} \end{pmatrix}. \tag{22}$$

The small-signal model of the system is shown in Fig. 3, encompassing the imaginary part, the real part, and the dc component. The control-to-output transfer function is

$$\boldsymbol{G_{\theta\_udc}}(s) = \boldsymbol{C}(s\boldsymbol{E} - \boldsymbol{A})^{-1}\boldsymbol{B}. \tag{23}$$

III. WIRELESS MOTOR SYSTEM STABILITY ANALYSIS

The state matrix $\boldsymbol{A}$ for the simplified model of the wireless motor system is third order. Based on (23), the characteristic equation of the system can be derived

$$a_0 s^3 + a_1 s^2 + a_2 s + a_3 = 0 \tag{24}$$

where

$$a_0 = 1, \qquad a_1 = \frac{8u_{\mathrm{dc0}}^2}{\pi^2 P L_\omega} + \frac{2R_{\mathrm{s}}}{L_\omega} - \frac{P}{u_{\mathrm{dc0}}^2 C_{\mathrm{dc}}},$$

$$a_2 = \frac{8u_{\mathrm{dc0}}^2}{\pi P L_\omega^2} + \frac{R_{\mathrm{s}}^2}{L_\omega^2} + \frac{8(1-\pi)}{\pi^2 L_\omega C_{\mathrm{dc}}} + \Delta\omega^2 - \frac{2PR_{\mathrm{s}}}{u_{\mathrm{dc0}}^2 L_\omega C_{\mathrm{dc}}},$$

$$a_3 = \frac{64u_{\mathrm{dc0}}^2}{\pi^3 P L_\omega^2 C_{\mathrm{dc}}} + \frac{8R_{\mathrm{s}}(1-\pi)}{\pi^2 L_\omega^2 C_{\mathrm{dc}}} - \frac{PR_{\mathrm{s}}^2}{u_{\mathrm{dc0}}^2 L_\omega^2 C_{\mathrm{dc}}} - \frac{P\Delta\omega^2}{u_{\mathrm{dc0}}^2 C_{\mathrm{dc}}}.$$

According to the Routh–Hurwitz criterion, for a third-order system to be stable, each term's coefficient should be positive and meet

$$a_1 \cdot a_2 > a_0 \cdot a_3. \tag{25}$$

It can be observed that the stability of the wireless motor system is mainly related to the motor power, the frequency deviation, the dc-link voltage, the equivalent inductance, the dc-link capacitance, and the secondary side coil resistance.

A. Influence of Input Parameters

Fig. 4 illustrates increasing motor power negatively affects the system's stability. As motor power increases, an RHP pole

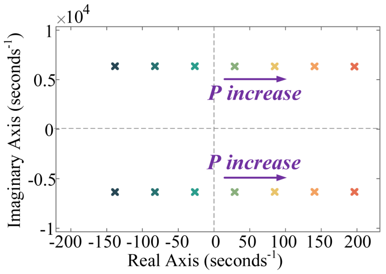

Fig. 4. Dominant pole–zero plot of motor power change.

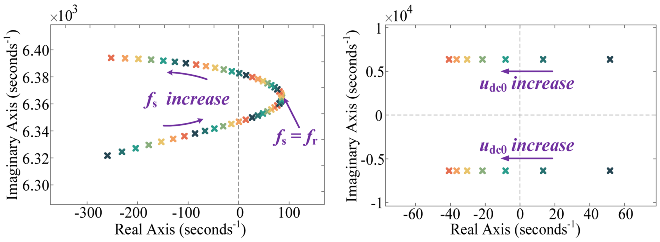

(a) (b)

Fig. 5. Dominant pole–zero plot of input parameters change. (a) Frequency change. (b) DC-link voltage change.

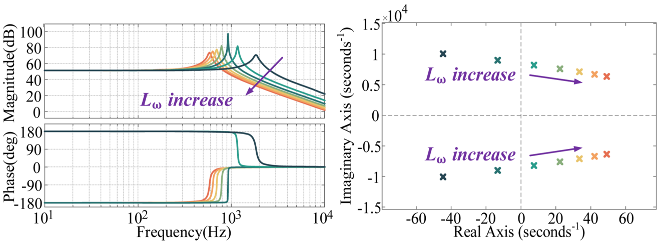

(a) (b)

Fig. 6. Frequency domain characteristics of the system when the equivalent inductance change. (a) Bode plot. (b) Pole–zero plot.

pair starts to emerge in the system's transfer function pole–zero plot, which results in a consistent decrease in system stability.

Fig. 5 depicts the effects of the system's operating frequency and dc-link voltage on the dominant pole pair of the system. As depicted in Fig. 5(a), an increase in the system's detuning level causes the dominant pole pair to shift to the left, indicating an enhancement in system stability. When the system is fully resonant, the dominant pole pair is situated at the extreme right, signifying a low level of system stability. Fig. 5(b) shows that an increase in dc-link voltage results in the leftward shift of the system's dominant pole pair, parallel to the real axis. This denotes an improvement in system stability, whereas the dynamic performance of the system remains largely unaffected. Nevertheless, as the leftward shift of the dominant pole pair, the influence of an increasing dc-link voltage on the position of the dominant pole pair gradually decreases. Additionally, a higher dc-link voltage may lead to increased switching losses in the motor driver.

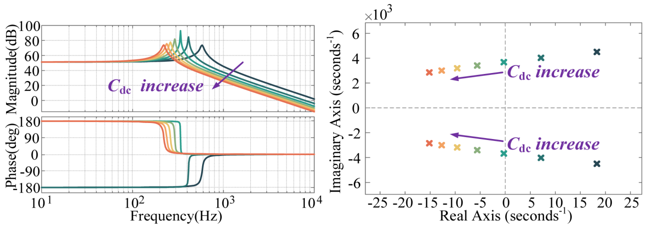

(a) (b)

Fig. 7. Frequency domain characteristics of the system when the DC-link capacitance changes. (a) Bode plot. (b) Pole–zero plot.

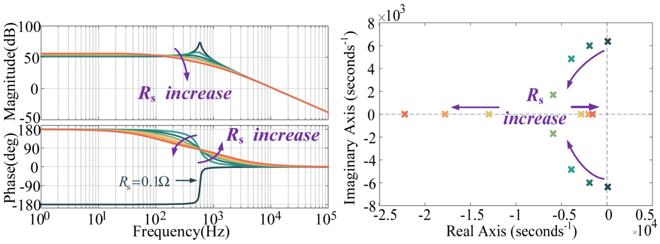

(a) (b)

Fig. 8. Frequency domain characteristics of the system when the secondary side coil internal resistance changes. (a) Bode plot. (b) Pole–zero plot.

B. Influence of Internal Parameters

Figs. 6–8 depict the Bode plot and the pole–zero plot, illustrating the effects of variations in the system's internal parameters. Fig. 6(a) demonstrates that as the equivalent inductance on the secondary side increases, the system's low-frequency gain largely stays constant, whereas both the corner frequency and crossover frequency decrease, leading to a narrower system bandwidth. Fig. 6(b) illustrates that, as the equivalent inductance increases, the dominant pole pair of the system shifts to the right and moves toward the real axis. This leads to a decreasing phase margin and reduced system stability.

Fig. 7(a) illustrates that as the dc-link capacitance increases, both the corner frequency and crossover frequency decrease, consequently reducing the system bandwidth. This indicates enhanced capabilities to attenuate high-frequency input perturbations. Fig. 7(b) depicts the dominant pole pair's movement to the left and toward the real axis, which indicates that an increase in dc-link capacitance can enhance system stability, albeit at the cost of the system's dynamic response speed.

Fig. 8(a) illustrates that as the secondary side coil internal resistance increases, the system's low-frequency gain and corner frequency remain constant, whereas the mid-frequency gain progressively decreases, consequently leading to an increase in system damping. Fig. 8(b) depicts the system's dominant pole pair gradually moving to the left and toward the real axis as the secondary side coil internal resistance increases, which results in improved system stability but a reduced system dynamic response speed.

In WPT systems, excessive resistance results in significant losses, thereby reducing the system's transmission efficiency. Therefore, it is generally recommended to keep the resistance

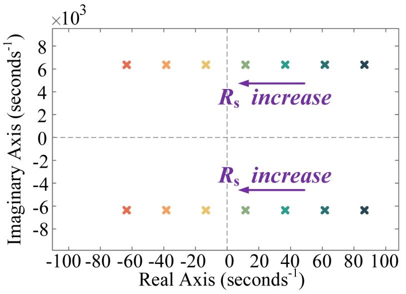

Fig. 9. Small amplitude adjustment of the secondary side coil internal resistance.

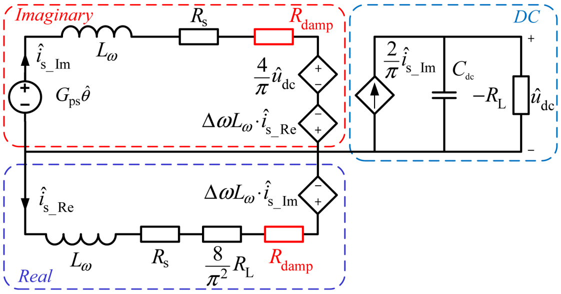

Fig. 10. Small-signal model of the system with a series virtual resistor.

within a small range. Fig. 9 shows the pole–zero plot as the secondary side coil internal resistance slightly increases. The dominant pole pair of the system is observed to shift leftward, parallel to the real axis, in response to an increase in the internal resistance of the secondary side coil. This indicates that the stability of the system can be effectively improved by adjusting the internal resistance of the secondary side coil in a small range, and the dynamic performance of the system will not be significantly affected.

IV. SECONDARY SIDE DAMPING RECONSTRUCTION CONTROL STRATEGY

Increasing the secondary side coil internal resistance is equivalent to adding a virtual resistance R_{damp} in series with the rectifier's input, as illustrated in Fig. 10. Therefore, the control block diagram of the system can be drawn as shown in Fig. 11(a), where K_1 represents the coupling relationship between the real and imaginary parts of the secondary side coil current. K_1 is expressed as

$$K_1 = \frac{\Delta\omega^2 L_\omega^2}{sL_\omega + R_{\mathrm{s}} + \frac{8}{\pi^2}R_{\mathrm{L}} + R_{\mathrm{damp}}}. \tag{26}$$

Through equivalent transformation, the virtual resistor R_{damp} can be converted into the system damping current i_{damp}, as shown in Fig. 11(b), where K_{damp} represents the small-signal gain from the dc-link voltage to the damping current. K_{damp} can be expressed as

$$K_{\mathrm{damp}} = \frac{sC_{\mathrm{dc}} - \frac{P}{u_{\mathrm{dc0}}^2}}{sL_\omega + R_{\mathrm{s}} + K_1}R_{\mathrm{damp}}. \tag{27}$$

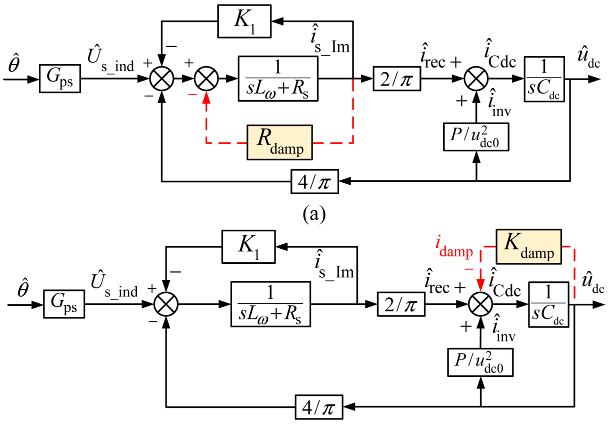

(a)

(b)

Fig. 11. Principle schematic of the control strategy. (a) Series virtual resistance. (b) Damping reconfiguration control method.

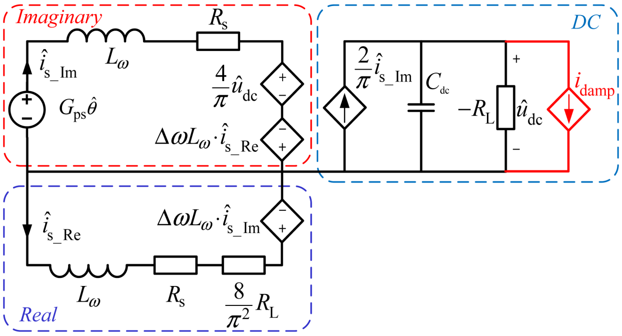

Fig. 12. Small-signal model of the DRC method.

As depicted in (27), K_{damp} is characterized as a transfer function correlated with the virtual resistance, which poses challenges for practical control implementation. Nevertheless, it is feasible to represent K_{damp} as a coefficient. Referring to Fig. 11(b), the small-signal model for the DRC method is explicated in Fig. 12. This leads to a transformation in the differential equation of the small-signal model on the bus side, articulated as follows:

$$C_{\mathrm{dc}}\frac{d\hat{u}_{\mathrm{dc}}}{dt} = \hat{i}_{\mathrm{rec}} + \frac{P}{u_{\mathrm{dc0}}^2}\cdot\hat{u}_{\mathrm{dc}} - K_{\mathrm{damp}}\cdot\hat{u}_{\mathrm{dc}}. \tag{28}$$

Notably, based on prior analysis, the stability of the system improves as the level of frequency detuning increases. In WPT systems, frequency detuning is generally undesirable, so satisfying the stability condition under no detuning, i.e., $\Delta\omega = 0$, is enough to ensure the system's stable operation.

When $\Delta\omega = 0$, the system's state matrix $\boldsymbol{A}$ changes to

$$\boldsymbol{A} = \begin{pmatrix} -\frac{8u_{\mathrm{dc0}}^2}{\pi^2 PL_\omega} - \frac{R_{\mathrm{s}}}{L_\omega} & 0 & 0 \\ 0 & -\frac{R_{\mathrm{s}}}{L_\omega} & -\frac{4}{\pi L_\omega} \\ 0 & \frac{2}{\pi C_{\mathrm{dc}}} & \frac{P}{u_{\mathrm{dc0}}^2 C_{\mathrm{dc}}} - \frac{K_{\mathrm{damp}}}{C_{\mathrm{dc}}} \end{pmatrix}. \tag{29}$$

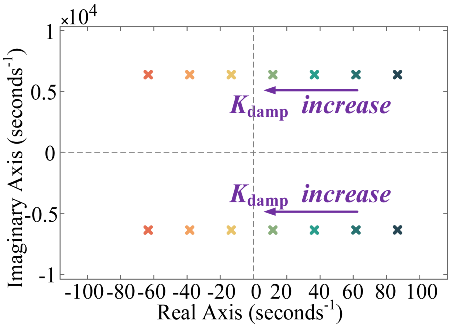

Fig. 13. Pole–zero plot of the system as K_{damp} increases.

The characteristic equation of the system is

$$b_0 s^2 + b_1 s + b_2 = 0 \tag{30}$$

where

$$b_0 = 1, \qquad b_1 = \frac{R_{\mathrm{s}}}{L_\omega} - \frac{P - K_{\mathrm{damp}} u_{\mathrm{dc0}}^2}{C_{\mathrm{dc}} u_{\mathrm{dc0}}^2},$$

$$b_2 = \frac{8u_{\mathrm{dc0}}^2 - \pi^2 P R_{\mathrm{s}} + \pi^2 u_{\mathrm{dc0}}^2 K_{\mathrm{damp}} R_{\mathrm{s}}}{C_{\mathrm{dc}} L_\omega}$$

.

According to the Routh–Hurwitz criterion, the range of values for K_{damp} to ensure system stability is

$$\begin{cases} K_{\mathrm{damp}} > \frac{P}{u_{\mathrm{dc0}}^2} - \frac{R_{\mathrm{s}} C_{\mathrm{dc}}}{L_\omega} \\ K_{\mathrm{damp}} > \frac{P}{u_{\mathrm{dc0}}^2} - \frac{8}{R_{\mathrm{s}} \pi^2} \end{cases}. \tag{31}$$

Fig. 13 shows the pole–zero plot of the system as K_{damp} increases. It can be observed that the DRC method can achieve a system stability improvement effect similar to that of adjusting the resistance. Typically, due to the low internal resistance of the secondary side coil, if the first expression in (31) holds true, then the second expression also holds true. Considering the parameter uncertainty in real systems, the value of K_{damp} should include a certain margin, which can be expressed as

$$K_{\mathrm{damp}} = \frac{1.5P}{u_{\mathrm{dc0}}^2} - \frac{R_{\mathrm{s}} C_{\mathrm{dc}}}{L_\omega}. \tag{32}$$

Since motor power can be obtained by sampling speed and *d*-*q* axis currents through internal sensors and calculated within the controller, DRC parameter K_{damp} can be adjusted in real-time based on motor power, ensuring the stability of the wireless motor system across its entire operating range.

The system shown in Fig. 12 requires a controlled current source in parallel on the dc link, which increases the complexity of the system and is relatively challenging to implement. In fact, the DRC method can be realized by improving the motor's control structure, as shown in Fig. 14. The following details the implementation method. The input power of the motor can be expressed as

$$P = u_{\mathrm{dc}} \cdot i_{\mathrm{inv}}. \tag{33}$$

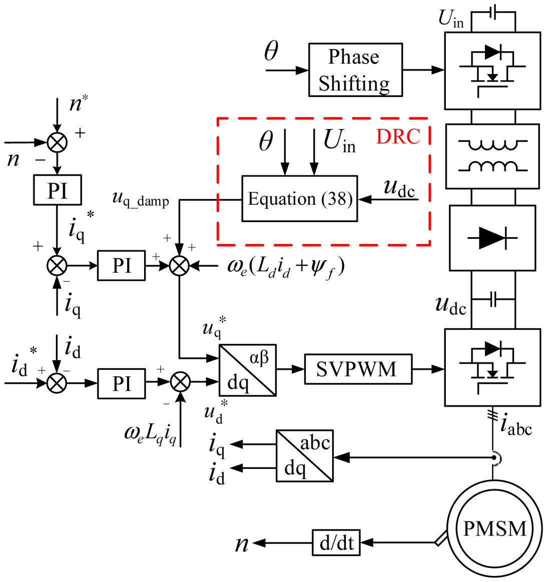

Fig. 14. Schematic diagram of the DRC method with *q*-axis voltage compensation.

The damping power P_{damp} generated by the damping current in the DRC method is

$$P_{\mathrm{damp}} = u_{\mathrm{dc}} \cdot i_{\mathrm{damp}} = u_{\mathrm{dc}} \cdot K_{\mathrm{damp}} \hat{u}_{\mathrm{dc}}. \tag{34}$$

The disturbance component of the dc-link voltage can be derived by calculating the difference between the actual and the steady-state values, expressed as

$$\hat{u}_{\mathrm{dc}} = u_{\mathrm{dc}} - u_{\mathrm{dc0}} = u_{\mathrm{dc}} - U_{\mathrm{in}} \omega^2 C_{\mathrm{p\_p}} M \cos\theta. \tag{35}$$

In the framework of constant amplitude transformation synchronous rotating coordinate system, the motor power can be articulately represented through the voltage and current parameters associated with the *q*-axis and the *d*-axis as follows:

$$P = 1.5\left(u_{\mathrm{q}} \cdot i_{\mathrm{q}} + u_{\mathrm{d}} \cdot i_{\mathrm{d}}\right). \tag{36}$$

Commonly, surface PMSMs adopt a control strategy with $i_{\mathrm{d}} = 0$ to ensure the stator current is minimized for the desired torque. This approach reduces copper losses and enhances efficiency. When disregarding motor and driver losses, the *d*-axis current approaches zero when the steady state is reached. Therefore, it can be inferred

$$P_{\mathrm{damp}} = 1.5 \cdot i_{\mathrm{q}} \cdot u_{\mathrm{q\_damp}}. \tag{37}$$

Combining (34), (35), and (37), the motor's *q*-axis damping voltage can be derived

$$u_{\mathrm{q\_damp}} = \frac{u_{\mathrm{dc}} \cdot K_{\mathrm{damp}} \left(u_{\mathrm{dc}} - U_{\mathrm{in}} \omega^2 C_{\mathrm{p\_p}} M \cos\theta\right)}{1.5 i_{\mathrm{q}}}. \tag{38}$$

At steady state, the small-signal component of the dc-link voltage and the *q*-axis damping voltage are both zero. Therefore, the DRC method reverts to the conventional motor control approach, and the addition of the DRC method does not impact the motor control system's static performance.

The small-signal admittance model of the motor drive system was modeled according to the method similar to that described in

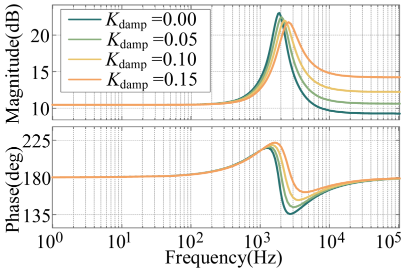

Fig. 15. Bode plot of the motor control system's small-signal impedance Z_{m} for different values.

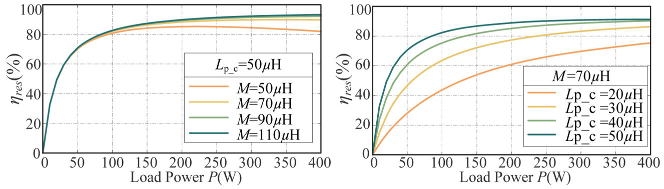

(a) (b)

Fig. 16. Influence of system parameters on resonator's efficiency trends. (a) Influence of load power on efficiency under varying M. (b) Influence of load power on efficiency with varying $L_{\mathrm{p\_c}}$.

TABLE I
SYSTEM PARAMETERS

Parameters	Value	Parameters	Value
$L_{\mathrm{p\_c}}$	50 μH	M	70 μH
$C_{\mathrm{p\_p}}$	1.26 μF	C_{s}	100 nF
$C_{\mathrm{p\_s}}$	250 nF	R_{p}	0.4 Ω
L_{p}	300 μH	R_{s}	0.4 Ω
L_{s}	600 μH	C_{dc}	60 μF

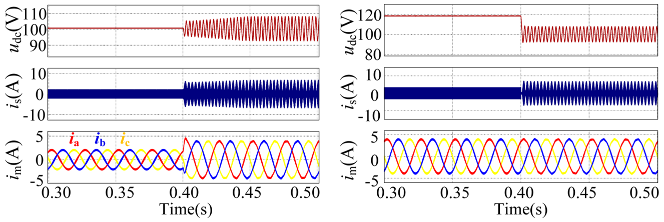

(a) (b)

Fig. 17. Influence of parameters change on system stability. (a) Motor power increases. (b) Input voltage decreases.

[8]. The detailed derivation process can be found in Appendix I. Fig. 15 shows the bode plot of the small-signal impedance model Z_{m} of the motor drive system for different K_{damp} values. At low frequencies, the DRC method has minimal effect on the system's dynamic performance. At mid frequencies, increasing K_{damp} smoothens the resonance peak, indicating that higher damping lessens the system's sensitivity at resonant frequencies, thereby improving stability. At high frequencies, as K_{damp} increases, the system's impedance increases, indicating that the effect of high-frequency voltage disturbances on the input current is mitigated. Typically, the frequency of disturbances in the dc link voltage is low, indicating that the DRC method has a slight impact on the dynamic performance of the motor driving system.

V. SIMULATION AND EXPERIMENTAL VERIFICATION

Simulations and experiments were conducted to validate the aforementioned analysis and the proposed control method. Due to the shortcomings such as the short lifespan and high failure rate of large-capacity electrolytic capacitors, this article utilized a 60 μF film capacitor as the dc-link capacitor in the wireless motor system. A trend graph depicting the influence of system parameters on the resonator's efficiency is presented in Fig. 16. The detailed analysis procedure is shown in Appendix II. As shown in Fig. 16(a), when the load power is low, the resonator's efficiency is virtually identical under different mutual inductances. However, as the load power increases, the system's efficiency declines with decreasing mutual inductance. Therefore, increasing the mutual inductance M will help improve the system's efficiency. However, in WPT systems, M is mainly affected by the transmission distance. In practical applications, M is usually small. Therefore, 70 μH was chosen as the mutual inductance for the magnetic coil. From Fig. 16(b), it can be observed that system efficiency increases with the increase of the compensation inductance $L_{\mathrm{p\_c}}$. However, a larger $L_{\mathrm{p\_c}}$ will increase the system's volume, which is disadvantageous for power density. Consequently, a compromise of 50 μH was chosen as the compensating inductance. On the other hand, Lower operating frequencies are more conducive to tuning, and the magnitude of the operating frequency does not impact the main innovative points proposed in this article. After comprehensive consideration, 20 kHz has been selected as the operating frequency for the system. The steady-state value of the system's dc-link voltage was set to 100 V. The inductances of the primary and secondary coils are 300 μH and 600 μH, respectively. Other system parameters can be calculated from (AII6) in Appendix II, as shown in Table I.

A. Simulation Analysis

The motor's reference speed was set to 1000 r/min, and simulations were conducted to assess the impact of output power and input voltage changes on the system's stability, as shown in Fig. 17. From Fig. 17(a), the system's output power is observed to increase with the escalating motor load torque. The system fails to meet stability conditions, exhibiting oscillations in the dc-link voltage and fluctuations in the secondary side coil current amplitude, indicating instability. Fig. 17(b) shows that when the input voltage is high, the dc-link voltage is also high, allowing the system to operate stably at high output power. As the input voltage decreases, the dc-link voltage reduces, accompanied by oscillations and fluctuations in the secondary side coil current amplitude, leading to system instability.

To verify the effectiveness of the proposed DRC method, simulation results are shown in Fig. 18. Without the DRC method, the system fails to meet stability conditions. This results in oscillations in the dc-link voltage and fluctuations in the

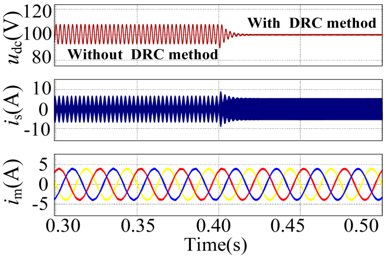

Fig. 18. Simulation result of the DRC method.

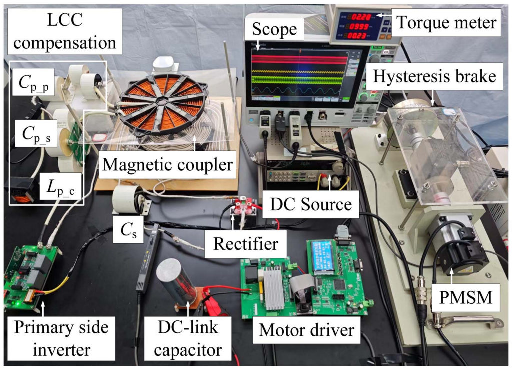

Fig. 19. Experimental platform.

secondary side coil current amplitude. Upon applying the DRC method, the system's damping is increased, and the dc-link voltage quickly stabilizes. Low-frequency oscillations in the dc-link voltage waveform and fluctuations in the secondary side coil current amplitude are eliminated.

B. Experimental Verification

To further validate the effectiveness of the proposed DRC method, a wireless motor system experimental platform was established, as shown in Fig. 19. The system parameters were the same as the simulation parameters, as shown in Table I.

The primary side input voltage of the wireless motor system was 100 V, provided by a programmable dc power supply. Phase shift modulation was implemented by the digital signal processor TMS320F28377. The rated power of the secondary-side motor in the wireless motor system is 250 W, with a rated torque of 2.4 N·m and a set speed of 1000 r/min. Its SVPWM modulation was implemented by the digital signal processor TMS320F8335, with a switching frequency of 10 kHz. The system load torque was provided by a hysteresis brake, with an output torque range of 0–4 N·m.

To verify the impact of the load power variation and the input voltage change on system stability, Fig. 20 illustrates the experimental waveforms under two conditions: increasing output power at a constant input voltage, and decreasing input voltage while maintaining a constant output power. The waveforms, from top to bottom, depict the primary side coil current, the dc-link voltage, the secondary side coil current, and the motor phase A current. As shown in Fig. 20(a), with the increase in load torque, the system's output power increases, whereas the primary side coil current remains essentially unchanged, and both the secondary side coil current and motor current amplitudes increase. Due to minor detuning and line resistance in the actual system, the dc-link voltage drops when the load torque increases, accompanied by more pronounced oscillations. Fig. 20(b) illustrates that as the input voltage decreases, the amplitude of the primary side coil current and dc-link voltage also decreases. With constant output power, the motor current amplitude remains unchanged, whereas the secondary side coil current amplitude increases, leading to oscillations in the dc-link voltage. These results indicate that the wireless motor system becomes unstable with either a decrease in input voltage or an increase in output power, manifesting oscillations in the dc-link voltage, consistent with the simulation results shown in Fig. 17.

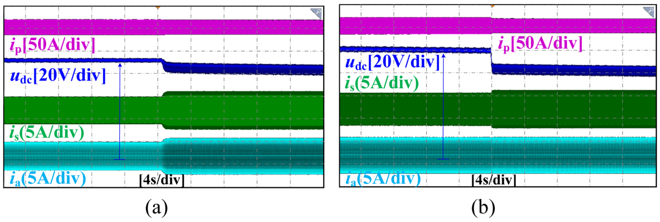

(a) (b)

Fig. 20. Experimental results on the impact of load power variation and input voltage change on system stability. (a) Increase in load torque. (b) Decrease in input voltage.

To validate the correctness of the stability conditions for the wireless motor system, Fig. 21 presents experimental results under three different load torque scenarios. Ignoring system detuning, the stability condition (25) can be simplified as

$$\begin{cases} \frac{R_s}{L_\omega} - \frac{P}{C_{dc}u_{dc0}^2} > 0 \\ \frac{8}{R_s\pi^2} - \frac{P}{u_{dc0}^2} > 0 \end{cases}. \tag{39}$$

Fig. 21(a) and (b) shows the experimental results for the motor at a set speed of 1000 r/min with load torques of 0.4 N·m and 1.4 N·m, respectively. It can be calculated that the motor's output power in these two scenarios is 42 W and 147 W, respectively, both satisfying the system's stability condition (39). Thus, within the system's stability range, the amplitude of the secondary side coil current escalates with an increase in output power, and the dc-link voltage remains stable. When the system load torque increases to 2.4 N·m, as shown in Fig. 21(c), the motor's output power reaches 251 W. As the system's stability condition (39) cannot be met, the dc-link voltage begins to exhibit oscillations with a peak-to-peak value of about 10 V. Meanwhile, the amplitude of the secondary side coil current fluctuates in response to the oscillations in the dc-link voltage.

To confirm the efficacy of the proposed control method, Fig. 22 presents the experimental results of the DRC method at a set speed of 1000 r/min and a load torque of 2.4 N·m. Fig. 22(a) illustrates the response of the wireless motor system after the implementation of the DRC method. The determination of K_{damp} can be achieved using the method outlined in Section IV, with a value of 0.018 in this condition. It can be observed that, upon applying the DRC method, the previous oscillations

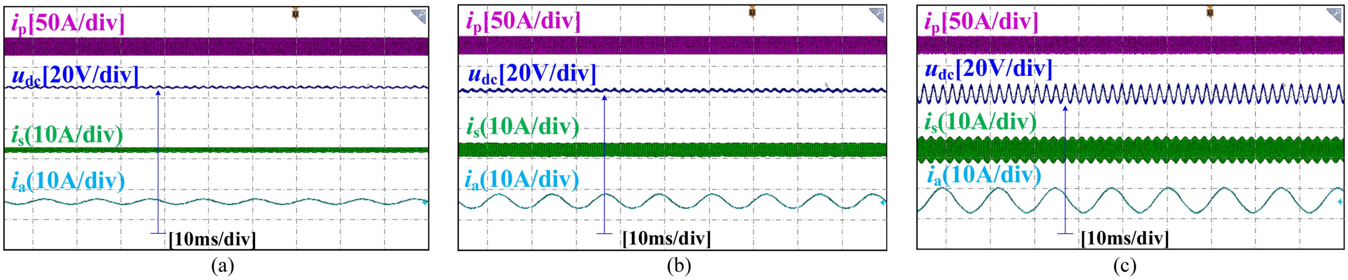

Fig. 21. Experimental results under three different load torque conditions. (a) 0.4 N·m load torque. (b) 1.4 N·m load torque. (c) 2.4 N·m load torque.

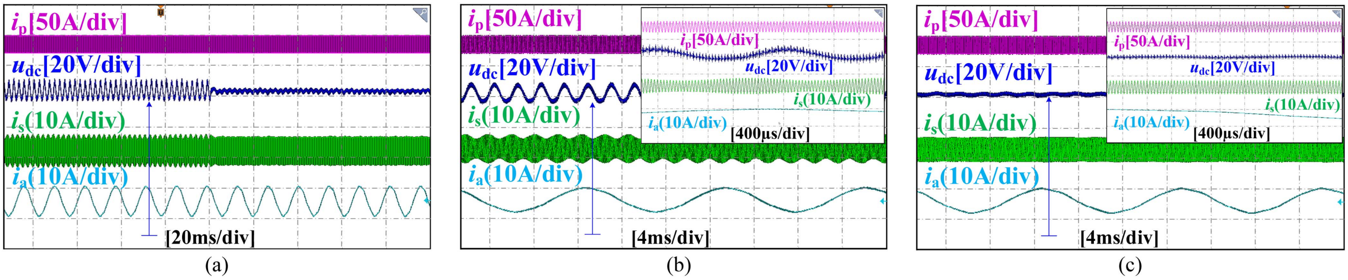

Fig. 22. Experimental results of the proposed DRC method. (a) System response after the implementation of the DRC method. (b) System waveform without the DRC method. (c) System waveform with the DRC method.

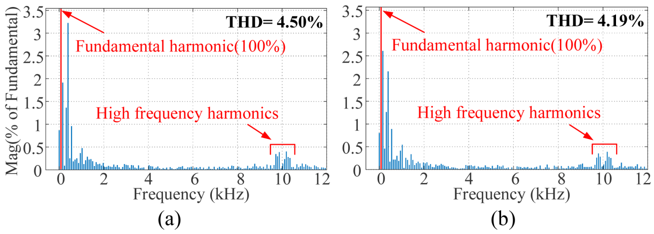

Fig. 23. Fourier analysis results of the motor stator current i_a. (a) Without the DRC method. (b) With the DRC method.

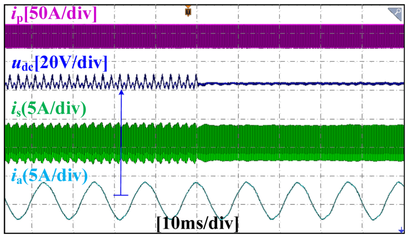

Fig. 24. Experimental results with the load torque of 2.4 N·m and the DC-link capacitance of 20 μF.

in the dc-link voltage quickly converge, and fluctuations in the secondary side coil current vanish, transitioning the system from an unstable to a stable state, in line with the simulation results shown in Fig. 18. Fig. 22(b) and (c) depicts the system waveforms without and with the DRC method, respectively. Fig. 22(b) shows that without the DRC method, a low-frequency component is superimposed on the switching ripple of the dc-link voltage, oscillating at 534 Hz, which approximates the resonant frequency of the secondary side equivalent inductance L_ω and the dc-link capacitor C_dc. Fig. 22(c) indicates that with the DRC method, the low-frequency component in the dc-link voltage is eliminated, retaining only the high-frequency ripple components generated by the secondary side rectifier and the three-phase inverter. These results demonstrate that the proposed DRC method can effectively suppress the oscillations in the dc-link voltage in the wireless motor system when stability conditions are not met, significantly enhancing system stability.

On the other hand, Fourier analysis was performed on the motor phase A current i_a data in the experimental results, as shown in Fig. 23. It can be seen that the THD value of i_a without the DRC method is 4.50%, whereas with the DRC method, it is 4.19%, indicating that the DRC method can reduce the harmonic content of i_a. In addition, the high-frequency harmonics of i_a are primarily concentrated around the switching frequency (10 kHz), and the introduction of the DRC method does not affect the high-frequency harmonic content of i_a.

To verify the effectiveness of the DRC method under different dc-link capacitance conditions, Fig. 24 presents the experimental results with a load torque of 2.4 N·m and a dc-link capacitance set at 20 μF. It is observed that without the DRC method, the system fails to meet the stability criteria, resulting in oscillations in the dc-link voltage and the secondary side coil current. Due to the reduction in the dc-link capacitance, the frequency of these oscillations increased to 925 Hz, higher than the oscillation frequency when the dc-link capacitance was 60 μF. The determination of K_damp can be achieved using the method outlined in Section IV, with a value of 0.031 in this condition. It can be seen that after implementing the DRC method, the oscillations in both the dc-link voltage and the secondary side coil current are effectively suppressed, indicating that the proposed DRC

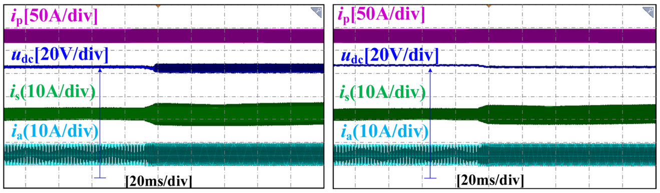

(a) (b)

Fig. 25. Experimental waveforms for the motor speed increasing from 500 to 1000 r/min. (a) Without DRC method. (b) With DRC method.

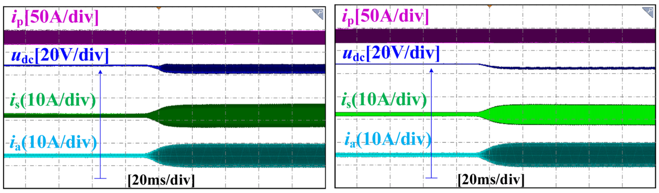

(a) (b)

Fig. 26. Experimental waveforms for the motor torque increasing from 0.4 to 2.4 N·m. (a) Without DRC method. (b) With DRC method.

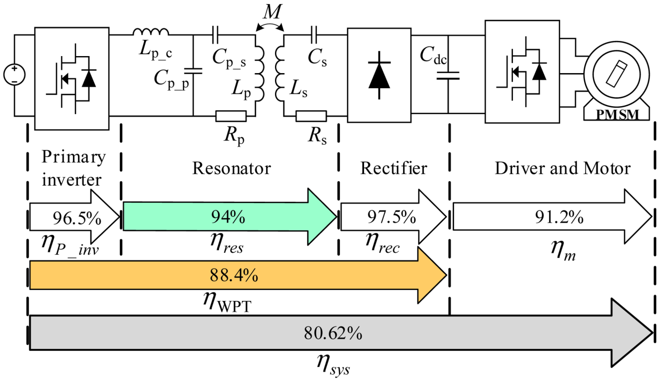

Fig. 27. Efficiency of each component in the wireless motor system at a load power of 250 W.

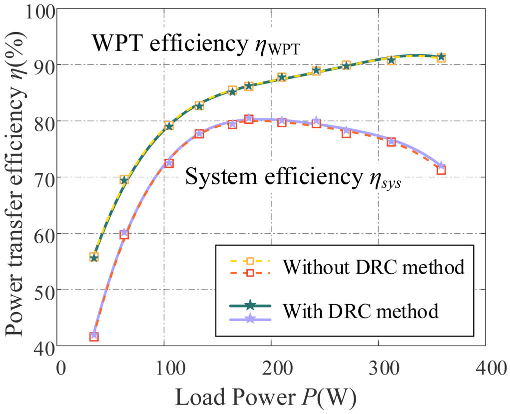

Fig. 28. Efficiency comparison with and without the DRC strategy.

method can effectively reduce the demand for dc-link capacitance in wireless motor systems.

To comprehensively validate the efficacy of the DRC method, variable speed and torque experiments were added to contrast the system responses in conditions with and without the DRC strategy, as depicted in Figs. 25 and 26. Fig. 25 shows the system response for a torque of 2.4 N·m, with speed increasing from 500 to 1000 r/min. It can be observed that, without the DRC method, the system is stable at the 500 r/min condition. When the speed increases to 1000 r/min, significant oscillations occur in the dc-link voltage, and the system cannot stabilize. With the introduction of the DRC method, stability is maintained at both the 500 r/min and 1000 r/min conditions, without significant compromise to the system's dynamic characteristics. Fig. 26 presents the system response for a speed of 1000 r/min, with torque increasing from 0.4 to 2.4 N·m. Similarly, without the DRC method, the system is stable at the 0.4 N·m condition. Upon increasing the torque to 2.4 N·m, significant oscillations in the dc-link voltage occur, rendering the system unstable. With the DRC method applied, the system remains stable at both the 0.4 and 2.4 N·m conditions. The experimental results thoroughly validate that the proposed DRC method effectively addresses stability concerns in wireless motor systems under unstable operational states.

The efficiency experiment of various components of the wireless motor system at a load power of 250 W is depicted in Fig. 27. The efficiency from the power source to the secondary dc-link η_{WPT} is 88.4%. The motor drive system's efficiency η_{m} is 91.2%, and the overall efficiency of the wireless motor system η_{sys} is 80.62%. On the other hand, Fig. 28 presents the efficiency of the WPT system and the wireless motor system, with and without the DRC method. It can be observed that the efficiency curves with the DRC method and without the DRC method are nearly identical, suggesting that the proposed DRC method has no impact on the efficiency of the wireless motor system.

At present, the DRC method proposed in this article is mainly applied in situations with low rotational speeds, such as inspection robots and industrial transport platforms, but cannot be applied in the motor's constant power operating region. Subsequent research will focus on the electric vehicle sector, investigating the stability of wireless power systems in the constant power operation region of motors.

VI. CONCLUSION

This article introduces a DRC method, designed to tackle instability issues in wireless motor systems. These issues become particularly pronounced under conditions of decreased input voltage or increased output power. The circuit simplification and modeling of the wireless motor system revealed that a slight increase in the secondary side coil internal resistance can significantly enhance the system's stability without compromising its dynamic performance. To address the additional power loss caused by the increase in resistance, the required resistance is transformed into dc side damping current, thereby equivalently enhancing the system's damping. This method effectively improves system stability when it is difficult to ensure stability through parameter design methods, such as increasing the capacitance value. Furthermore, this method can effectively reduce the system's demand for the dc-link capacitance values. Simulation and experimental results demonstrate that the proposed DRC method can effectively suppress the oscillations in dc-link voltage caused by the system's inability to meet stability conditions when the input voltage is reduced or the output power is increased, significantly enhancing the system's stability.

APPENDIX I

The motor's *d*-*q* axis voltage is represented as

$$\begin{bmatrix} u_\mathrm{d} \\ u_\mathrm{q} \end{bmatrix} = \begin{bmatrix} r_\mathrm{s} + sL_\mathrm{d} & -\omega_\mathrm{e} L_\mathrm{q} \\ \omega_\mathrm{e} L_\mathrm{d} & r_\mathrm{s} + sL_\mathrm{q} \end{bmatrix} \begin{bmatrix} i_\mathrm{d} \\ i_\mathrm{q} \end{bmatrix} + \begin{bmatrix} 0 \\ \omega_\mathrm{e} \psi_f \end{bmatrix} \tag{AI1}$$

where u_d, u_q, i_d, i_q, L_d, and L_q, respectively, represent the actual voltage, current, and inductance on the *d*-*q* axis. ω_e is the motor's angular velocity, r_s is the stator resistance, and ψ_f is the flux of the permanent magnet.

The small-signal components of the *d*-*q* axis voltage are

$$\begin{bmatrix} \hat{u}_\mathrm{d} \\ \hat{u}_\mathrm{q} \end{bmatrix} = \begin{bmatrix} r_\mathrm{s} + sL_\mathrm{d} & -\omega_\mathrm{e} L_\mathrm{q} \\ \omega_\mathrm{e} L_\mathrm{d} & r_\mathrm{s} + sL_\mathrm{q} \end{bmatrix} \begin{bmatrix} \hat{i}_\mathrm{d} \\ \hat{i}_\mathrm{q} \end{bmatrix}. \tag{AI2}$$

The relationship between the small-signal components of the motor's *d*-*q* axis voltage and the small-signal components of the dc-link voltage can be expressed as

$$\begin{bmatrix} \hat{u}_\mathrm{d} \\ \hat{u}_\mathrm{q} \end{bmatrix} = \frac{\hat{u}_\mathrm{dc}}{u_\mathrm{dc0}} \begin{bmatrix} u_\mathrm{d0} \\ u_\mathrm{q0} \end{bmatrix} + \begin{bmatrix} \hat{u}_\mathrm{dref} \\ \hat{u}_\mathrm{qref} \end{bmatrix} \tag{AI3}$$

where u_dc, u_dref, and u_qref, respectively, represent the dc-link voltage, the reference value for *d*-axis voltage, and the reference value for *q*-axis voltage.

Define the inner loop transfer functions for the *d*-*q* axis currents as

$$\begin{cases} G_\mathrm{d} = K_\mathrm{pd} + \frac{K_\mathrm{id}}{s} \\ G_\mathrm{q} = K_\mathrm{pq} + \frac{K_\mathrm{iq}}{s} \end{cases} \tag{AI4}$$

with the DRC method applied, the reference values for the motor's *d*-*q* axis voltages become

$$\begin{bmatrix} u_\mathrm{dref} \\ u_\mathrm{qref} \end{bmatrix} = \begin{bmatrix} -G_\mathrm{d} & -\omega_\mathrm{e} L_\mathrm{q} \\ \omega_\mathrm{e} L_\mathrm{d} & -G_\mathrm{q} \end{bmatrix} \begin{bmatrix} i_\mathrm{d} \\ i_\mathrm{q} \end{bmatrix} + \begin{bmatrix} G_\mathrm{d} i_\mathrm{dref} \\ G_\mathrm{q} i_\mathrm{qref} + \omega_\mathrm{e} \psi_f \end{bmatrix} + \begin{bmatrix} 0 \\ u_\mathrm{q\_damp} \end{bmatrix}. \tag{AI5}$$

The small-signal model is as follows:

$$\begin{bmatrix} \hat{u}_\mathrm{dref} \\ \hat{u}_\mathrm{qref} \end{bmatrix} = \begin{bmatrix} -G_\mathrm{d} & -\omega_\mathrm{e} L_\mathrm{q} \\ \omega_\mathrm{e} L_\mathrm{d} & -G_\mathrm{q} \end{bmatrix} \begin{bmatrix} \hat{i}_\mathrm{d} \\ \hat{i}_\mathrm{q} \end{bmatrix} + \begin{bmatrix} G_\mathrm{d} \hat{i}_\mathrm{dref} \\ G_\mathrm{q} \hat{i}_\mathrm{qref} \end{bmatrix} + \begin{bmatrix} 0 \\ \hat{u}_\mathrm{q\_damp} \end{bmatrix}. \tag{AI6}$$

According to (47), the small-signal component of the *q*-axis damping voltage is

$$\hat{u}_\mathrm{q\_damp} = \frac{K_\mathrm{damp} u_\mathrm{dc0}}{1.5 i_\mathrm{q0}} \hat{u}_\mathrm{dc}. \tag{AI7}$$

Assuming the current reference values are undisturbed, by combining (AI2), (AI3), (AI6), and (AI7), it can be concluded that

$$\begin{bmatrix} \hat{i}_\mathrm{d} \\ \hat{i}_\mathrm{q} \end{bmatrix} = \frac{\hat{u}_\mathrm{dc}}{u_\mathrm{dc0}} \begin{bmatrix} \frac{u_\mathrm{d0}}{r_\mathrm{s} + sL_\mathrm{d} + G_\mathrm{d}} \\ \frac{u_\mathrm{q0} + K_\mathrm{damp} u_\mathrm{dc0}^2 / (1.5 i_\mathrm{q0})}{r_\mathrm{s} + sL_\mathrm{q} + G_\mathrm{q}} \end{bmatrix}. \tag{AI8}$$

On the other hand, ignoring losses, the input and output power are equal

$$u_\mathrm{dc} i_\mathrm{inv} = 1.5(u_\mathrm{d} i_\mathrm{d} + u_\mathrm{q} i_\mathrm{q}) \tag{AI9}$$

where i_inv represent the inverter input current. The small-signal components of (AI9) are

$$\hat{u}_\mathrm{dc} i_\mathrm{inv0} + u_\mathrm{dc0} \hat{i}_\mathrm{inv} = 1.5(\hat{u}_\mathrm{d} i_\mathrm{d0} + u_\mathrm{d0} \hat{i}_\mathrm{d} + \hat{u}_\mathrm{q} i_\mathrm{q0} + u_\mathrm{q0} \hat{i}_\mathrm{q}). \tag{AI10}$$

Substituting (AI2) and (AI8) into (AI10) yields the small-signal input admittance of the motor control system with the DRC method as

$$\begin{aligned} Y_m(s) = Z_m^{-1}(s) = \frac{\hat{i}_\mathrm{inv}}{\hat{u}_\mathrm{dc}} &= -\frac{i_\mathrm{inv0}}{u_\mathrm{dc0}} \\ &+ \frac{3}{2} \frac{u_\mathrm{d0}}{u_\mathrm{dc0}^2} \times \frac{u_\mathrm{d0} + \omega_\mathrm{e} L_\mathrm{d} i_\mathrm{q0} + sL_\mathrm{d} i_\mathrm{d0} + i_\mathrm{d0} r_\mathrm{s}}{r_\mathrm{s} + sL_\mathrm{d} + G_\mathrm{d}} \\ &+ \frac{3}{2} \left(\frac{u_\mathrm{q0}}{u_\mathrm{dc0}^2} + \frac{K_\mathrm{damp}}{1.5 i_\mathrm{q0}} \right) \\ &\times \frac{u_\mathrm{q0} + \omega_\mathrm{e} L_\mathrm{q} i_\mathrm{d0} + sL_\mathrm{q} i_\mathrm{q0} + i_\mathrm{q0} r_\mathrm{s}}{r_\mathrm{s} + sL_\mathrm{q} + G_\mathrm{q}}. \end{aligned} \tag{AI11}$$

APPENDIX II

The steady-state equivalent model of the wireless motor system is shown in Fig. 29, where U_p, I_1, I_p, I_s, and U_s, respectively, represent the output voltage and output current of the primary side inverter, primary coil current, secondary coil current, and secondary rectifier input voltage. R_e represents the equivalent load of the motor load R_L converted to the ac side

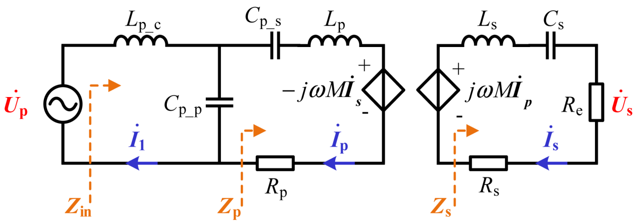

Fig. 29. Steady-state equivalent model of the wireless motor system.

$$R_\mathrm{e} = \frac{8}{\pi^2} R_\mathrm{L} = \frac{U_\mathrm{s}^2}{P}. \tag{AII1}$$

Hence, the secondary current I_s is

$$I_\mathrm{s} = \frac{P}{U_\mathrm{s}}. \tag{AII2}$$

Based on Fig. 29, the secondary impedance $\mathbf{Z_s}$, primary impedance $\mathbf{Z_p}$, and input impedance $\mathbf{Z_{in}}$ can be expressed as follows:

$$\boldsymbol{Z_s} = j\omega L_{\mathrm{s}} + \frac{1}{j\omega C_{\mathrm{s}}} + R_{\mathrm{e}} + R_{\mathrm{s}} \tag{AII3}$$

$$\boldsymbol{Z_p} = j\omega L_{\mathrm{p}} + \frac{1}{j\omega C_{\mathrm{p\_s}}} + \frac{\omega^2 M^2}{Z_{\mathrm{s}}} + R_{\mathrm{p}} \tag{AII4}$$

$$\boldsymbol{Z_{in}} = j\omega L_{\mathrm{p\_c}} + \frac{1}{j\omega C_{\mathrm{p\_p}} + 1/Z_{\mathrm{p}}}. \tag{AII5}$$

The resonance condition for the LCC-S compensation topology is

$$\begin{cases} j\omega L_{\mathrm{p\_c}} + \frac{1}{j\omega C_{\mathrm{p\_p}}} = 0 \\ j\omega L_{\mathrm{p}} + \frac{1}{j\omega C_{\mathrm{p\_s}}} + \frac{1}{j\omega C_{\mathrm{p\_p}}} = 0 \\ j\omega L_{\mathrm{s}} + \frac{1}{j\omega C_{\mathrm{s}}} = 0 \end{cases}. \tag{AII6}$$

Combining (AII3) and (AII6) yields

$$|\boldsymbol{Z_{in}}| = \frac{\omega^2 L_{\mathrm{p\_c}}^2 (R_{\mathrm{e}} + R_{\mathrm{s}})}{R_{\mathrm{p}} R_{\mathrm{e}} + R_{\mathrm{p}} R_{\mathrm{s}} + \omega^2 M^2}. \tag{AII7}$$

Therefore, the input current and input power of the resonator are as follows:

$$I_1 = \frac{U_{\mathrm{p}}}{|\boldsymbol{Z_{in}}|} = U_{\mathrm{p}} \frac{R_{\mathrm{p}} R_{\mathrm{e}} + R_{\mathrm{p}} R_{\mathrm{s}} + \omega^2 M^2}{\omega^2 L_{\mathrm{p\_c}}^2 (R_{\mathrm{e}} + R_{\mathrm{s}})} \tag{AII8}$$

$$P_{\mathrm{in}} = U_{\mathrm{p}} I_1 = U_{\mathrm{p}}^2 \frac{R_{\mathrm{p}} R_{\mathrm{e}} + R_{\mathrm{p}} R_{\mathrm{s}} + \omega^2 M^2}{\omega^2 L_{\mathrm{p\_c}}^2 (R_{\mathrm{e}} + R_{\mathrm{s}})}. \tag{AII9}$$

According to Fig. 29, the primary coil current can be expressed as

$$I_{\mathrm{p}} = I_1 \left| \frac{1/j\omega C_{\mathrm{p\_p}}}{1/j\omega C_{\mathrm{p\_p}} + Z_{\mathrm{p}}} \right| = \frac{U_{\mathrm{p}}}{\omega L_{\mathrm{p\_c}}}. \tag{AII10}$$

Thus, the secondary coil induced voltage is

$$U_{\mathrm{s\_ind}} = \omega M I_{\mathrm{p}} = \frac{M U_{\mathrm{p}}}{L_{\mathrm{p\_c}}}. \tag{AII11}$$

Simultaneously, it can be represented as

$$U_{\mathrm{s\_ind}} = U_{\mathrm{s}} + \frac{P}{U_{\mathrm{s}}} R_{\mathrm{s}}. \tag{AII12}$$

Combining (AII11) and (AII12) yields two solutions

$$\begin{cases} U_{\mathrm{s\_1}} = \frac{1}{2}\left(\frac{M U_{\mathrm{p}}}{L_{\mathrm{p\_c}}} - \frac{\sqrt{M^2 U_{\mathrm{p}}^2 - 4 L_{\mathrm{p\_c}}^2 P R_{\mathrm{s}}}}{L_{\mathrm{p\_c}}}\right) \\ U_{\mathrm{s\_2}} = \frac{1}{2}\left(\frac{M U_{\mathrm{p}}}{L_{\mathrm{p\_c}}} + \frac{\sqrt{M^2 U_{\mathrm{p}}^2 - 4 L_{\mathrm{p\_c}}^2 P R_{\mathrm{s}}}}{L_{\mathrm{p\_c}}}\right) \end{cases}. \tag{AII13}$$

The first solution in (AII13) approaches zero, which is not feasible. Hence, it can be derived as

$$U_{\mathrm{s}} = \frac{1}{2}\left(\frac{M U_{\mathrm{p}}}{L_{\mathrm{p\_c}}} + \frac{\sqrt{M^2 U_{\mathrm{p}}^2 - 4 L_{\mathrm{p\_c}}^2 P R_{\mathrm{s}}}}{L_{\mathrm{p\_c}}}\right). \tag{AII14}$$

The input power of the resonator is

$$P_{\mathrm{in}} = U_{\mathrm{p}} I_1 = U_{\mathrm{p}}^2 \frac{R_{\mathrm{p}} U_{\mathrm{s}}^2/P + R_{\mathrm{p}} R_{\mathrm{s}} + \omega^2 M^2}{\omega^2 L_{\mathrm{p\_c}}^2 (U_{\mathrm{s}}^2/P + R_{\mathrm{s}})}. \tag{AII15}$$

The efficiency of the resonator is

$$\eta_{res} = U_{\mathrm{p}}^2 \frac{R_{\mathrm{p}} U_{\mathrm{s}}^2/P + R_{\mathrm{p}} R_{\mathrm{s}} + \omega^2 M^2}{\omega^2 L_{\mathrm{p\_c}}^2 (U_{\mathrm{s}}^2/P + R_{\mathrm{s}})} \times 100\%. \tag{AII16}$$

REFERENCES

[1] H. Woo, P. Jang-Hyun, C. Joo, H. Ahn, D. Kang, and T. Kim, "Analysis of the transformer characteristics for an integration system with a wireless power transfer device and linear motor," *Energies*, vol. 14, no. 20, May 2021, Art. no. 6769.

[2] M. Sato, G. Yamamoto, D. Gunji, T. Imura, and H. Fujimoto, "Development of wireless in-wheel motor using magnetic resonance coupling," *IEEE Trans. Power Electron.*, vol. 31, no. 7, pp. 5270–5278, Jul. 2016.

[3] W. Liu, K. T. Chau, C. H. T. Lee, L. Cao, and W. Han, "Wireless power and drive transfer for piping network," *IEEE Trans. Ind. Electron.*, vol. 69, no. 3, pp. 2345–2356, Mar. 2022.

[4] W. Han, K. T. Chau, Z. Hua, and H. Pang, "Compact wireless motor drive using orthogonal bipolar coils for coordinated operation of robotic arms," *IEEE Trans. Magn.*, vol. 58, no. 2, Feb. 2022, Art. no. 8200608.

[5] N. Ali, Z. Liu, H. Armghan, and A. Armghan, "Super-twisting sliding mode controller for maximum power transfer efficiency tracking in hybrid energy storage based wireless in-wheel motor," *Sustain. Energy Technol. Assessments*, vol. 52, Feb. 2022, Art. no. 102075.

[6] K. Pietilainen, L. Harnefors, A. Petersson, and H.-P. Nee, "DC-link stabilization and voltage sag ride-through of inverter drives," *IEEE Trans. Ind. Electron.*, vol. 53, no. 4, pp. 1261–1268, Jun. 2006.

[7] M. Hinkkanen and J. Luomi, "Induction motor drives equipped with diode rectifier and small DC-link capacitance," *IEEE Trans. Ind. Electron.*, vol. 55, no. 1, pp. 312–320, Jan. 2008.

[8] Y. A. I. Mohamed, A. A. A. Radwan, and T. K. Lee, "Decoupled reference-voltage-based active dc-link stabilization for PMSM drives with tight-speed regulation," *IEEE Trans. Ind. Electron.*, vol. 59, no. 12, pp. 4523–4536, Dec. 2012.

[9] M. Cespedes, L. Xing, and J. Sun, "Constant-power load system stabilization by passive damping," *IEEE Trans. Power Electron.*, vol. 26, no. 7, pp. 1832–1836, Jul. 2011.

[10] X. Liu, Y. Zhou, W. Zhang, and S. Ma, "Stability criteria for constant power loads with multistage *LC* filters," *IEEE Trans. Veh. Technol.*, vol. 60, no. 5, pp. 2042–2049, Jun. 2011.

[11] X. Zhang, X. Ruan, H. Kim, and C. K. Tse, "Adaptive active capacitor converter for improving stability of cascaded dc power supply system," *IEEE Trans. Power Electron.*, vol. 28, no. 4, pp. 1807–1816, Apr. 2013.

[12] X. Chang, Y. Li, X. Li, and X. Chen, "An active damping method based on a supercapacitor energy storage system to overcome the destabilizing effect of instantaneous constant power loads in dc microgrids," *IEEE Trans. Energy Convers.*, vol. 32, no. 1, pp. 36–47, Mar. 2017.

[13] X. Zhang, D. M. Vilathgamuwa, K. Tseng, B. S. Bhangu, and C. J. Gajanayake, "Power buffer with model predictive control for stability of vehicular power systems with constant power loads," *IEEE Trans. Power Electron.*, vol. 28, no. 12, pp. 5804–5812, Dec. 2013.

[14] W. Du, J. Zhang, Y. Zhang, and Z. Qian, "Stability criterion for cascaded system with constant power load," *IEEE Trans. Power Electron.*, vol. 28, no. 4, pp. 1843–1851, Apr. 2013.

[15] X. Zhang, Q. Zhong, V. Kadirkamanathan, J. He, and J. Huang, "Source-side series-virtual-impedance control to improve the cascaded system stability and the dynamic performance of its source converter," *IEEE Trans. Power Electron.*, vol. 34, no. 6, pp. 5854–5866, Jun. 2019.

[16] M. N. Hussain, R. Mishra, and V. Agarwal, "A frequency-dependent virtual impedance for voltage-regulating converters feeding constant power loads in a dc microgrid," *IEEE Trans. Ind. Appl.*, vol. 54, no. 6, pp. 5630–5639, Nov./Dec. 2018.

[17] O. Lorzadeh, I. Lorzadeh, M. N. Soltani, and A. Hajizadeh, "Source-side virtual *RC* damper-based stabilization technique for cascaded systems in DC microgrids," *IEEE Trans. Energy Convers.*, vol. 36, no. 3, pp. 1883–1895, Sep. 2021.

[18] S. Liu, P. Su, and L. Zhang, "A virtual negative inductor stabilizing strategy for dc microgrid with constant power loads," *IEEE Access*, vol. 6, pp. 59728–59741, 2018.

[19] X. Liu, A. J. Forsyth, and A. M. Cross, "Negative input-resistance compensator for a constant power load," *IEEE Trans. Ind. Electron.*, vol. 54, no. 6, pp. 3188–3196, Dec. 2007.

[20] P. Liutanakul, A. B. Awan, S. Pierfederici, B. Nahid-Mobarakeh, and F. Meibody-Tabar, “Linear stabilization of a dc bus supplying a constant power load: A general design approach,” *IEEE Trans. Power Electron.*, vol. 25, no. 2, pp. 475–488, Feb. 2010.
[21] R. Maheshwari, S. Munk-Nielsen, and K. Lu, “An active damping technique for small dc-link capacitor based drive system,” *IEEE Trans. Ind. Inform.*, vol. 9, no. 2, pp. 848–858, May 2013.
[22] J. Huo, N. Zhao, G. Wang, G. Zhang, L. Zhu, and D. Xu, “An active damping control method for reduced dc-link capacitance PMSM drives with low line inductance,” *IEEE Trans. Power Electron.*, vol. 37, no. 12, pp. 14328–14342, Dec. 2022.
[23] N. Zhao, G. Wang, D. Ding, G. Zhang, and D. Xu, “Impedance based stabilization control method for reduced dc-link capacitance IPMSM drives,” *IEEE Trans. Power Electron.*, vol. 34, no. 10, pp. 9879–9890, Oct. 2019.
[24] D. Wang, K. Lu, P. O. Rasmussen, L. Mathe, Y. Feng, and F. Blaabjerg, “Voltage modulation using virtual positive impedance concept for active damping of small dc-link drive system,” *IEEE Trans. Power Electron.*, vol. 33, no. 12, pp. 10611–10621, Dec. 2018.
[25] X. Zhang, X. Ruan, and Q.-C. Zhong, “Improving the stability of cascaded dc/dc converter systems via shaping the input impedance of the load converter with a parallel or series virtual impedance,” *IEEE Trans. Ind. Electron.*, vol. 62, no. 12, pp. 7499–7512, Dec. 2015.
[26] X. Zhang, Q.-C. Zhong, and W.-L. Ming, “Stabilization of a cascaded dc converter system via adding a virtual adaptive parallel impedance to the input of the load converter,” *IEEE Trans. Power Electron.*, vol. 31, no. 3, pp. 1826–1832, Mar. 2016.
[27] X. Zhang, Q.-C. Zhong, and W.-L. Ming, “Stabilization of cascaded dc/dc converters via adaptive series-virtual-impedance control of the load converter,” *IEEE Trans. Power Electron.*, vol. 31, no. 9, pp. 6057–6063, Sep. 2016.
[28] P. Magne, D. Marx, B. Nahid-Mobarakeh, and S. Pierfederici, “Large-signal stabilization of a dc-link supplying a constant power load using a virtual capacitor: Impact on the domain of attraction,” *IEEE Trans. Ind. Appl.*, vol. 48, no. 3, pp. 878–887, May/Jun. 2012.
[29] W.-J. Lee and S.-K. Sul, “DC-link voltage stabilization for reduced dc-link capacitor inverter,” *IEEE Trans. Ind. Appl.*, vol. 50, no. 1, pp. 404–414, Jan./Feb. 2014.
[30] M. Wu and D. Lu, “Active stabilization methods of electric power systems with constant power loads: A review,” *J. Mod. Power Syst. Clean Energy*, vol. 2, no. 3, pp. 233–243, Jul. 2014.
[31] H. Li, J. Fang, and Y. Tang, “Dynamic phasor-based reduced-order models of wireless power transfer systems,” *IEEE Trans. Power Electron.*, vol. 34, no. 11, pp. 11361–11370, Nov. 2019.

Shuai Dong was born in Shandong Province, China, in 1987. He received the M.S. and Ph.D. degrees in electrical engineering from Harbin Institute of Technology (HIT), Harbin, China, in 2011 and 2016, respectively.

In 2017, he joined the Institute of Wireless Power Transfer Technology, HIT, where he is currently an Associate Professor. His research interests include wireless power transfer technology and power electronics converter topologies and control.

Yuebo Chen was born in Henan, China, in 1999. He received the M.S. degree in electrical engineering in 2023 from the Harbin Institute of Technology, Harbin, China, where he is currently working toward the Ph.D. degree in electrical engineering.

His research interests include wireless power transfer technology and wireless motor technology.

Xiangyu Chen was born in Henan, China, in 2000. He received the B.S. degree in electrical engineering from Harbin University of Science and Technology, Harbin, China, in 2022. He is currently working toward the Ph.D. degree in electrical engineering with Harbin Institute of Technology, Harbin, China.

His research interests include wireless power transfer and wireless motor control.

Baichuan Zhang was born in Hebei, China, in 1997. He received the M.S. degree in electrical engineering in 2022 from the Harbin Institute of Technology, Harbin, China, where he is currently working toward the Ph.D. degree in electrical engineering.

His research interests include wireless power transfer technology and power electronics technology.

Chunbo Zhu received the B.S. and M.S. degrees in electrical engineering and the Ph.D. degree in mechanical engineering from the Harbin Institute of Technology (HIT), Harbin, China, in 1987, 1992, and 2001, respectively.

From 2003 to 2004, he was a postdoctoral research fellow with the PEI Research Center, National University of Ireland, Galway, Ireland. Since 1987, he has been a Lecturer with the Department of Automation Measurement and Control, HIT. He is currently a full Professor with HIT, where he leads the Laboratory of Wireless Power Transfer and Battery Management Technologies. His research interests include energy management systems, electric and hybrid electric vehicles, and wireless power transfer technologies.